THERMOELECTRIC POWER OF $Hg_{2.86}AsF_6$

THERMOELECTRIC POWER OF $Hg_{2.86}AsF_6$

By

Günter Adolf Scholz, B.Sc.

A Thesis

Submitted to the School of Graduate Studies

in Partial Fulfilment of the Requirements

for the Degree

Master of Science

McMaster University

February, 1977

für meine Mutter

MASTER OF SCIENCE (1977)   McMaster University
(Physics)   Hamilton, Ontario

TITLE: Thermoelectric Power of $Hg_{2.86}AsF_6$

AUTHOR: Günter Adolf Scholz, B.Sc. (Simon Fraser University)

SUPERVISOR: Dr. W.R. Datars

NUMBER OF PAGES: ix, 46

ABSTRACT

An apparatus was developed to measure the Seebeck e.m.f. of small specimens which have to be handled in a dry-box and to which only mechanical contact can be made. The method is successful if the electrical conductivity of the contacts is much larger than that of the sample. Utilizing this apparatus, the temperature dependence of the thermopower of $Hg_{2.86}AsF_6$ was investigated along its two principal directions. Metallic conduction was found which is electron dominated in the $\hat{a},\hat{b}$ directions and hole dominated in the $\hat{c}$ direction. Therefore, the temperature dependence observed in the thermopower is explained using the free electron model, in which the total thermopower is expressed as the sum of a diffusion component, dominating above 100 K, and a phonon drag component dominating below 100 K. Thus, the Fermi energy is calculated to be 4.6 ± 0.5 eV and the Debye temperature is fixed between 60 K and 90 K.

iv

ACKNOWLEDGMENTS

TABLE OF CONTENTS

LIST OF FIGURES

LIST OF TABLES

Textbooks and Heaven only are Ideal

Solidity is an imperfect state.

Within the cracked and dislocated Real

Nonstoichiometric crystals dominate.

Stray Atoms sully and precipitate;

Strange holes, exitons, wander loose; because

of Dangling Bonds, a chemical Substrate

Corrodes and catalyzes - surface Flaws

Help Epitaxial Growth to fix adsorptive claws.

John Updike

(The Dance of the Solids)

CHAPTER I

Introduction

There has been considerable interest in quasi-one-dimensional systems because they exhibit a wide range of properties (Little, 1964; Peierls, 1955; Coleman et al., 1973). They may be metals, dielectrics, high T_c superconductors, or show transport properties such as a metal-insulator transition, depending on the number of particles and the character of the interaction between them. So far most of the attention has been focussed on the organic charge transfer compounds (Chaikin, 1973; Kwak, 1976), $(SN)_x$ and the tetracyanoplatinate complexes (Schuster, 1974).

Another very promising compound is $Hg_{2.86}AsF_6$ (Cutforth et al., 1975). It consists of $(AsF_6)^-$ octahedra at tetragonal lattice points, with an array of non-intersecting channels along the $\hat{a}$, $\hat{b}$ directions which contain chains of mercury atoms. The interchain distance along the $\hat{a}$ and $\hat{b}$ axes is 7.54 Å and 3.08 Å along the $\hat{c}$ axis. The intrachain mercury-mercury distances are 2.5 Å to 2.7 Å, which are incommensurate with the $(AsF_6)^-$ lattice (Brown et al., 1974). $Hg_{2.86}AsF_6$ satisfies the requirements of a pseudo-one-dimensional conductor because

    i)   the mercury atoms are arranged in linear, non-intersecting chains,

    ii)   the intrachain mercury-mercury distance is very small,

resulting in a large transfer integral,

iii) and there is a formal charge transfer of about 0.35 electrons per mercury atom to the $(AsF_6)^-$ anions so that a partially filled conduction band is formed.

Electrical conductivity measurements from 4.2 K to 300 K have shown a room-temperature conductivity of 10^4 $(\Omega \cdot cm)^{-1}$ and a resistance ratio $(R_{300}/R_{4.2})$ of at least 10^3 in the high conductivity direction (Cutforth et al., 1975). This amply confirms the compound's metallic nature. Optical reflectivity and electrical conductivity measurements have shown that the anisotropy ratio between the $\hat{a}$, $\hat{b}$ directions and the $\hat{c}$ direction has a lower limit of 10 and an upper limit of 200 (Cutforth et al., 1976; Batalla, 1976). However, several problems were encountered in performing the above measurements. $Hg_{2.86}AsF_6$ is very difficult to handle because it is extremely hygroscopic and exposure to about 10 p.p.m. of water changes its surface properties within minutes. Furthermore, the one-dimensional chains are extremely sensitive to defects and imperfections, so that it is difficult to grow large single crystals that are suitable for electrical or optical measurements.

The Seebeck coefficient, which is investigated in this work, is a sensitive transport property that is not critically dependent on crystal quality. That is to say, it is a bulk effect which is independent of sample geometry and it is a zero-current measurement so that small discontinuities are not important if there is only a small fraction of the total temperature drop across them.

CHAPTER II

Preparation and Crystal Structure

$Hg_{2.86}AsF_6$ is prepared by the direct reaction of a solution of $Hg_3(AsF_6)_2$ in SO_2 with elemental mercury (Cutforth et al., 1975). $Hg_3(AsF_6)_2$ is prepared by the disproportionation of $Hg_4(AsF_6)_2$, which in turn is made by the direct reaction of elemental mercury with AsF_5.

The reaction vessel is shown in Figure 2.1. By cooling the arm containing elemental mercury with liquid nitrogen and heating the other, the solution will transfer to the mercury side. After several days at $-35°C$, the golden, distinctly metallic, crystalline solid $Hg_{2.86}AsF_6$ grows on the mercury surface. Crystals are subsequently isolated by manouvering any excess mercury close to the sintered plug, transferring the solution into the other arm and then sealing the tube at S.

The crystal data are summarized in Table 2.1 (Brown et al., 1974). These results are essentially those reported previously, except for the intrachain mercury-mercury distance which is not constant at the average value of 2.64 Å, but varies randomly between 2.5 Å and 2.7 Å. This is quite reasonable since every mercury atom experiences a different chemical environment. An isometric view of the crystal structure is given in Figure 2.2. The tetragonal lattice consists of $(AsF_6)^-$ octa- hedra belonging to the space group $I4_1/amd$. The non-intersecting channels,

3

FIGURE 2.1:   Growth tube for $Hg_{2.86}AsF_6$.

FIGURE 2.2:   Isometric view of $Hg_{2.86}AsF_6$ showing the chains of
mercury atoms (circles) in the $(AsF_6)^-$ (octahedra)
lattice.

sintered
glass plug

S

solution of
$Hg_3(AsF_6)_2$
in SO_2

mercury

agitator

C

b

a
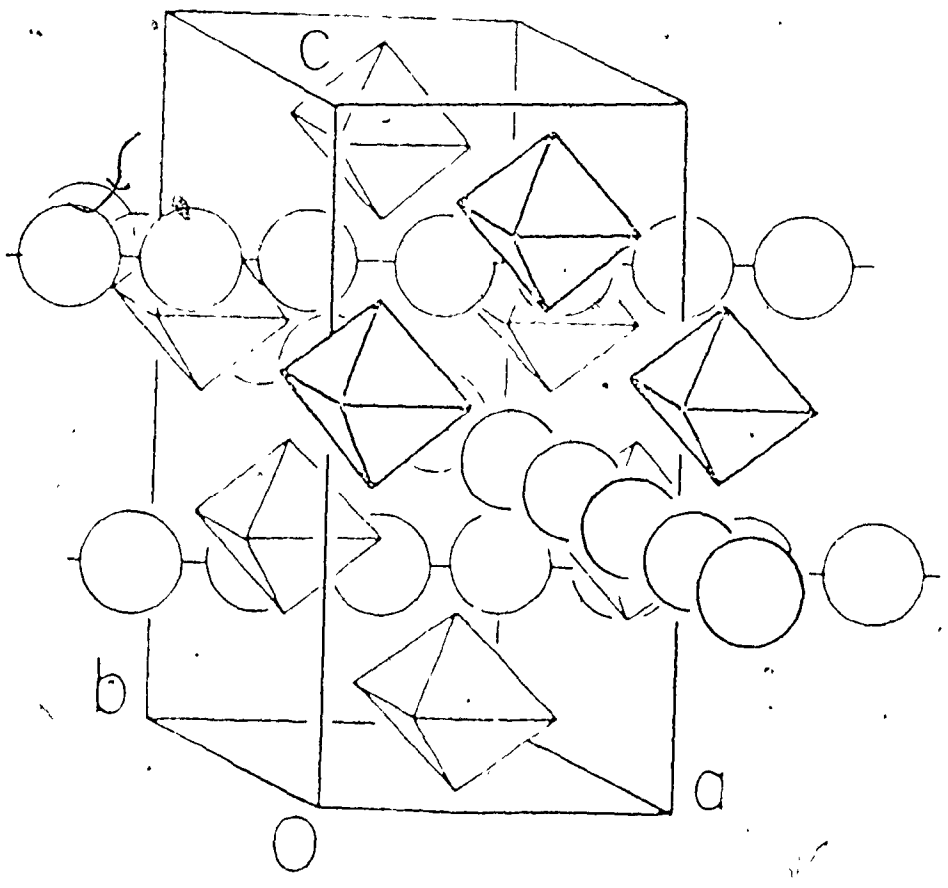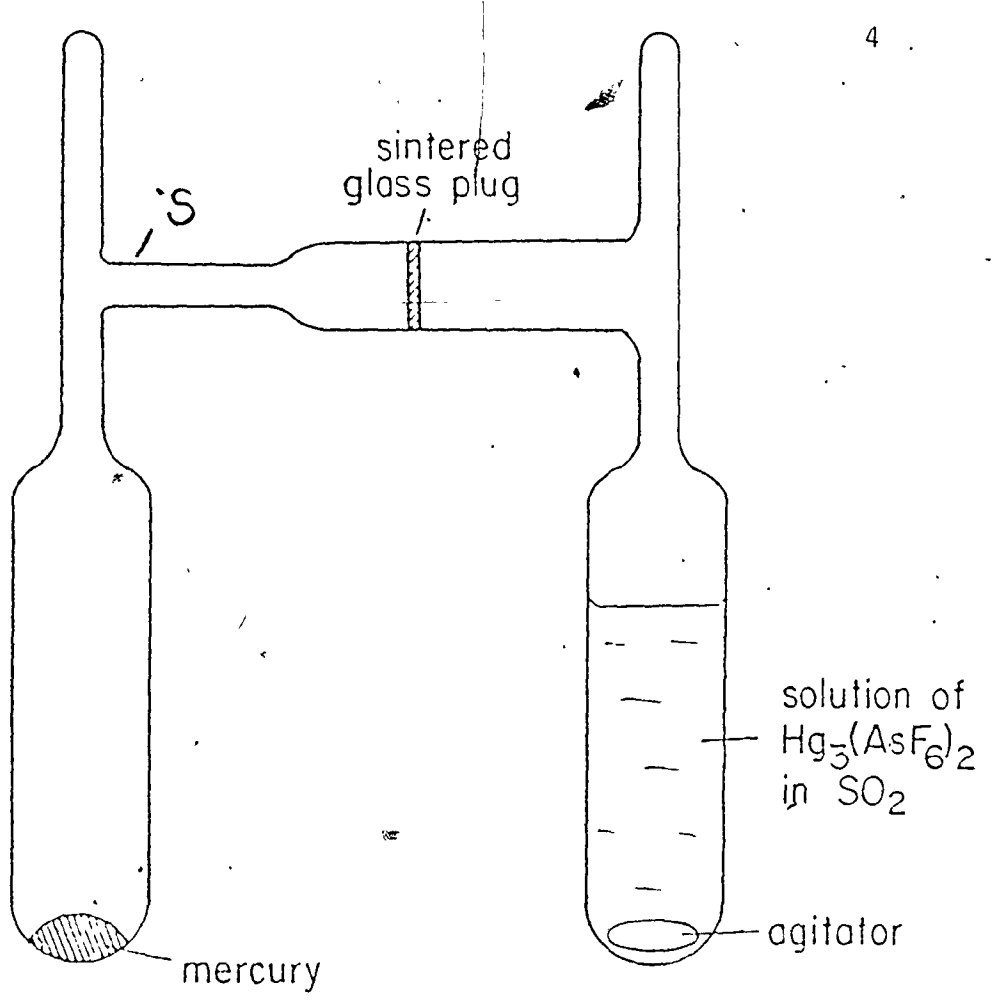
running along the $\hat{a}$ and $\hat{b}$ directions, are filled with mercury atoms whose separation is incommensurate with respect to the lattice. It should be noted that the interatomic separation for elemental mercury is 3.00 Å (Barrett, 1957) which is considerably greater than the intrachain mercury distance and only slightly less than the interchain distance along the $\hat{c}$ axis. Also, it should be mentioned that the mercury atoms in one chain are not ordered in any way with respect to the mercury atoms in any other chain.

TABLE 2.1:   Crystal data for $Hg_{2.86}AsF_6$.

Intrachain mercury distances

average   2.64 Å

actual   random within
                                                   2.5 Å and 2.7 Å

Interchain distances

â and b̂   7.54 Å

ĉ   3.08 Å

As-F distances   1.69 Å; 1.71 Å

Crystalline Hg-Hg distances   3.00 Å

F$^-$ radius   1.3 Å

System   tetragonal

Space group $I4_1/amd$

Cell volume   701.1 Å^3

Formula weight   573.7

Number of formula
units per unit cell   4

CHAPTER III

Theory

When we place a conductor in a thermal gradient, the electrons and/or holes at the hot end will acquire additional energy relative to the cold end and will diffuse toward the cold end. This diffusion takes place until there is dynamic equilibrium with the electrostatic repulsion due to the excess charge at the cold end. Electrical connections made to measure the resulting e.m.f., introduce another e.m.f. because of the thermal gradient along the electrical leads. From Figure 3.1 we may in general write the voltage that is detected as

$$V_{BA}(T_0,T_1,T_2) = V_A(T_1,T_2) - V_B(T_0,T_1,T_2). \tag{1}$$

V_{BA} is called the Seebeck e.m.f. after its discoverer, Johann Seebeck (1780-1831). The Seebeck voltage $V_{BA} = -V_{AB}$ is referred to as positive when the terminal at the colder end is positive with respect to the warmer end. The thermopower S_{BA} is defined as

$$S_{BA} = \lim_{\Delta T \to 0} \frac{V_{BA}}{\Delta T}. \tag{2}$$

where $\Delta T = T_2 - T_1$.

An advantage of using the thermoelectric effect is that it is independent of the geometry of the material except possibly at extremely low temperatures, when the mean free path of the electrons becomes as

7

large as the dimensions of the conductor. However, it is not possible to measure V_A directly since the circuit has to be made of at least two different materials to have a net e.m.f.

The absolute thermopower of each conductor may be determined from the electrochemical potentials $\bar{\mu}$ indicated in Figure 3.1. The electro-chemical potential is the sum of the chemical and the electrostatic potentials, that is

$$\bar{\mu} = \mu - |e| \, V. \tag{3}$$

When both conductors at a junction are at the same temperature and there is no current, the electrochemical potential is continuous across the junction. Therefore

$$\bar{\mu}_B(T_1) = \bar{\mu}_A(T_1)$$

$$\bar{\mu}_B(T_2) = \bar{\mu}_A(T_2). \tag{4}$$

Now, let us use Eq. (17) from the transport theory, which will be discussed in the following pages, to relate the absolute thermopower S to the electro-chemical potential. Eq. (17) yields

$$\int d\bar{\mu} = |e| \int S dT. \tag{5}$$

with the current density $\vec{J} = 0$. For junctions (3), (2), (1), Eq. (5) is

$$\bar{\mu}_B(T_0) - \bar{\mu}_B(T_2) = |e| \int_{T_2}^{T_0} S_B dT$$

$$\bar{\mu}_A(T_2) - \bar{\mu}_A(T_1) = |e| \int_{T_1}^{T_2} S_A dT \tag{6}$$

FIGURE 3.1:   Simple arrangement for measuring a Seebeck e.m.f.

$V_A (T_2, T_1)$

T_1 $\bar{\mu}_A(T_1)$ A $\bar{\mu}_A(T_2)$ T_2

$\bar{\mu}_B(T_1)$ (1)   (2) $\bar{\mu}_B(T_2)$

$V_B^I(T_0, T_1)$ $V_B(T_0, T_2)$

B   B

$\bar{\mu}_B''(T_0)$ (3) $\bar{\mu}_B(T_0)$

T_0

$V_{BA}(T_0, T_2, T_1)$

Detector
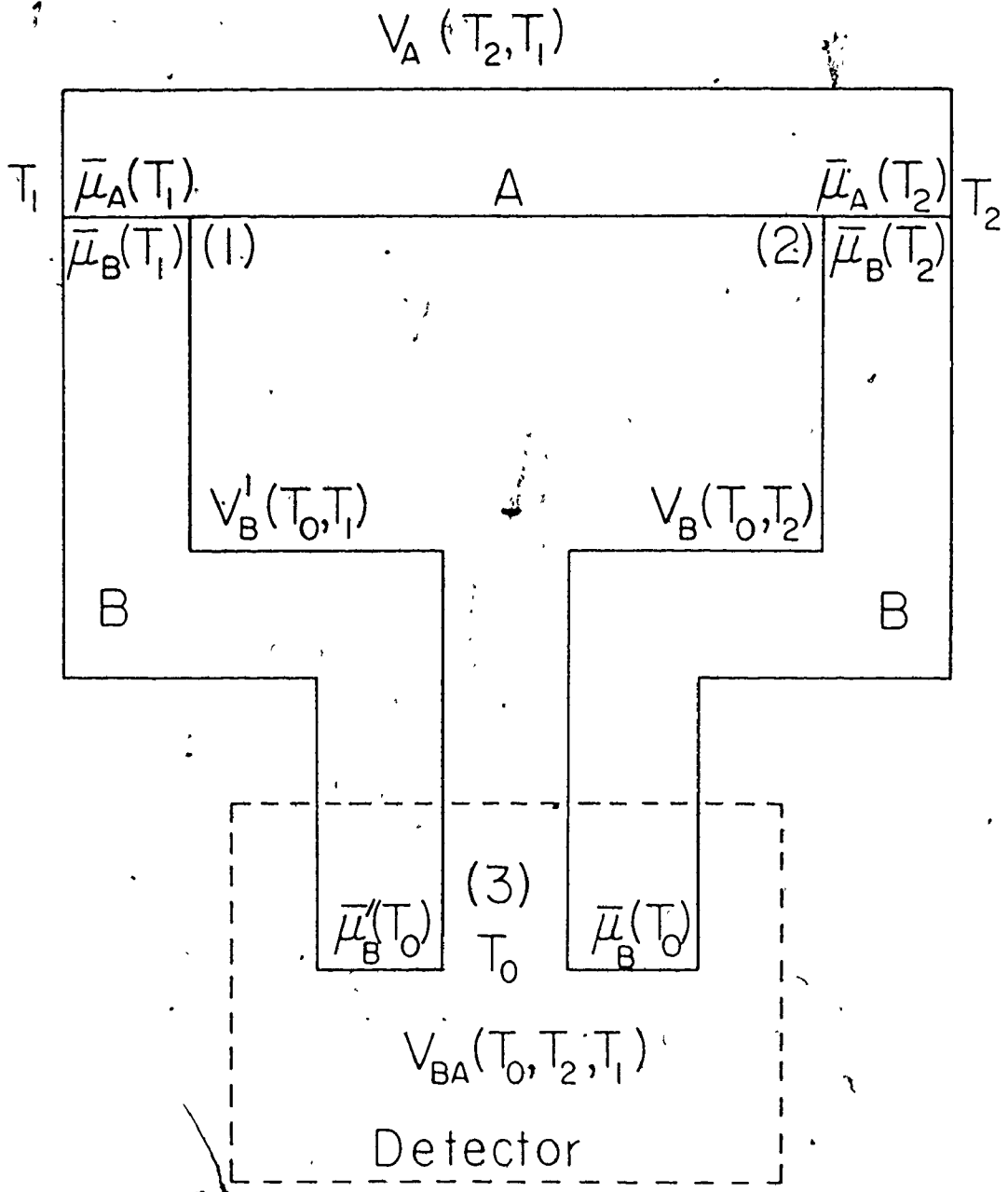
$$\bar{\mu}_B(T_1) - \bar{\mu}_B'(T_0) = |e| \int_{T_0}^{T_1} S_B dT.$$

Adding the three equations of (6) and making use of Eq. (4) we get

$$\bar{\mu}_B(T_0) - \bar{\mu}_B'(T_0) = |e| \int_{T_1}^{T_2} S_A dT + |e| \int_{T_2}^{T_1} S_B dT$$

or

$$\bar{\mu}_B(T_0) - \bar{\mu}_B'(T_0) = |e| \int_{T_1}^{T_2} (S_A - S_B) dT. \tag{7}$$

Since the chemical components $\mu_B(T_0) = \mu_B'(T_0)$, for identical materials, we may rewrite Eq. (7) as

$$\{\mu_B(T_0) - |e| V_B(T_0)\} - \{\mu_B'(T_0) - |e| V_B'(T_0)\}$$

$$= |e| \int_{T_1}^{T_2} (S_A - S_B) dT$$

giving

$$V_B'(T_0) - V_B(T_0) = \int_{T_1}^{T_2} (S_A - S_B) dT. \tag{8}$$

Of course, $\{V_B'(T_0) - V_B(T_0)\}$, which is clearly independent of T_0, is the Seebeck potential V_{BA}. Differentiating Eq. (8) and using Eq. (2), we are finally able to write

$$\frac{dV_{BA}}{dT} = S_{BA} = S_A - S_B. \tag{9}$$

The thermopower of the couple BA is just the difference in the absolute thermopower of its components A and B.

Many authors have given derivations of the thermopower in terms of the microscopic and macroscopic transport equations. In the following brief outline, results are freely quoted from "Thermoelectricity in Metals and Alloys" by R.D. Barnard (1972).

A set of linear macroscopic transport equations between small forces (F_j) and their respective flows (X_i) is written as

$$X_i = \sum_{j=1}^{n} a_{ij}F_j. \quad (i = 1, .., n) \tag{10}$$

Diagonal coupling coefficients ($i=j$) may be identified with primary forces causing primary flows. For example, electric potential gradients causing electron currents. The coefficients with $i \neq j$ measure interference effects such as an electric potential gradient causing a heat flux. Furthermore, it can be shown (de Groot, 1951) that at the molecular level

$$a_{ij} = a_{ji}. \tag{11}$$

We need to consider two forces resulting from the temperature gradients and the electric potentials to determine the thermopower so that

$$X_1 = a_{11}F_1 + a_{12}F_2$$
$$X_2 = a_{12}F_1 + a_{22}F_2. \tag{12}$$

There is, however, considerable difficulty in choosing the correct flows for the forces. Careful considerations show that a compatible set of flows and forces are

$$\vec{J} = b_{11} \frac{\vec{\nabla}\mu}{T} + b_{12} \frac{\vec{\nabla}T}{T^2}$$

$$\vec{J}_Q = b_{12} \frac{\vec{\nabla}\mu}{T} + b_{22} \frac{\vec{\nabla}T}{T^2} .$$

(13)

where $\vec{J}$ is the electron current density and $\vec{J}_Q$ is the heat flux. It should be clearly understood that (13) represents a convenient, but not unique choice of matching flows and forces. Now, we are in a position to express the coupling coefficients in terms of experimentally measurable quantities. For example, the electrical conductivity under isothermal conditions is given by

$$\vec{I} = -|e|\vec{J} = -\sigma\vec{\nabla}V .$$

(14)

Then from (3) and (13) with $\vec{\nabla}T = 0$ we obtain

$$\vec{J} = \frac{b_{11}}{T} (\vec{\nabla}\mu - |e|\vec{\nabla}V) .$$

(15)

and since $\vec{\nabla}\mu = 0$ in an isothermal environment, we can combine this with (14) to obtain

$$b_{11} = - \frac{\sigma T}{e^2} .$$

(16)

Use of the same type of technique for the other coefficients allows us to express the Onsager transport equations (13) in terms of experimental variables in the form

$$\vec{J} = - \frac{\sigma}{e^2} \vec{\nabla}\mu + \frac{\sigma}{|e|} S \vec{\nabla}T$$

$$\vec{J}_Q = \frac{\sigma}{|e|} ST\vec{v}\vec{\mu} - (\kappa + \sigma S^2 T)\vec{\nabla} T. \tag{17}$$

where κ is the thermal conductivity. For comparative purposes later on, let us rewrite the first equation in Eq. (17) as.

$$\vec{I} = -\sigma\vec{\nabla}V - \sigma(S - \frac{1}{|e|} \frac{\partial\mu}{\partial T})\vec{\nabla}T. \tag{18}$$

We can write a generalized expression for $\vec{I}$ as

$$\vec{I} = -|e| \int \vec{v}dN. \tag{19}$$

where N is the number of conduction electrons per unit volume and $\vec{v}$ is the electron drift velocity. The number of occupied states in $\vec{k}$-space is

$$dN = \frac{1}{4\pi^3} f(\vec{k},\vec{r})d\vec{k}. \tag{20}$$

where $f(\vec{k},\vec{r})$ is the Fermi-Dirac distribution function, which for free electrons having $E = \hbar^2 k^2/2m$ becomes

$$dN = \frac{1}{2\pi^2} (\frac{2m}{h^2})^{3/2} \quad f(E,\vec{r})E^{1/2}dE. \tag{21}$$

Thus

$$\vec{I} = \frac{e}{2\pi^2} (\frac{2m}{\hbar^2})^{3/2} \int \vec{v}\, f(E,\vec{r})E^{1/2}dE. \tag{22}$$

The distribution function is evaluated by assuming a characteristic

relaxation time such that

$$f(t) = f_0 + f(t=0)e^{-t/\tau}.$$ (23)

where $f(t=0)$ is the steady state distribution function. Since the interactions causing the relaxation are collisions, we write

$$\left.\frac{\partial f}{\partial t}\right)_{collisions} = -\frac{1}{\tau}(f - f_0).$$ (24)

The rate of change of f under an applied potential gradient is

$$\left.\frac{\partial f}{\partial t}\right)_{\vec{v}} = \frac{e}{m}\vec{E}\cdot\vec{\nabla}_{\vec{v}} f + \vec{v}\cdot\vec{\nabla}_{\vec{r}} f + \frac{\partial f}{\partial t}.$$ (25)

where $\vec{E}$ is the electric field and use is made of

$$\frac{d\vec{v}}{dt} = \frac{e}{m}\vec{E}.$$ (26)

If we now assume a steady state exists under the action of temperature and/or potential gradients, we must have

$$\left.\frac{\partial f}{\partial t}\right)_{\vec{v}} = \left.\frac{\partial f}{\partial t}\right)_{collisions}; \quad \frac{\partial f}{\partial t} = 0.$$ (27)

Thus,

$$\frac{e}{m}\vec{E}\cdot\vec{\nabla}_{\vec{v}} f + \vec{v}\cdot\vec{\nabla}_{\vec{r}} f = -\frac{1}{\tau}(f - f_0).$$ (28)

The simplest approximate solution to this can be obtained if we assume f does not differ greatly from f_0 and write

$$f = f_0 - \tau(\frac{e}{m} \vec{E} \cdot \vec{\nabla}_{\vec{v}} f_0 + \vec{v} \cdot \vec{\nabla}_{\vec{r}} f_0). \tag{29}$$

If we rewrite $\vec{v}$ in Eq. (29) in terms of E using $E = \frac{1}{2} mv^2$ and substitute this into Eq. (22) we obtain

$$\vec{I} = \frac{-e}{2\pi^2} (\frac{2m}{\hbar^2})^{3/2} \int \frac{2E^{2/3}}{3m} \tau[e\vec{E} \frac{\partial f_0}{\partial} + \vec{\nabla} f_0]dE. \tag{30}$$

where f_0 is ignored, because the equilibrium distribution does not cause any current flow. Instead of dealing with $\vec{\nabla} f_0$ in Eq. (30), it will be considerably more satisfying to express it in terms of $\vec{\nabla}T$. In fact

$$\vec{\nabla} f_0 = \frac{\partial f_0}{\partial T} \vec{\nabla} T. \tag{31}$$

However, since $\frac{\partial f_0}{\partial E}$ is used already in Eq. (30), we will write Eq. (31) as

$$\vec{\nabla} f_0 = - \frac{\partial f_0}{\partial E} (\frac{E-E_F}{T} + \frac{\partial E_F}{\partial T}) \vec{\nabla} T. \tag{32}$$

which on substitution into Eq. (30) gives

$$\vec{I} = e^2 H_1 \vec{E} + |e| [(\frac{\partial E_F}{\partial T} - \frac{E_F}{T})H_1 + \frac{H_2}{T}] \vec{\nabla} T. \tag{33}$$

where

$$H_n = - \frac{16\pi\sqrt{2m}}{3h^3} \int \tau E^{n+1/2} \frac{\partial f_0}{\partial E} dE. \tag{34}$$

This finally expresses the current density due to an electric potential

and/or temperature gradient of a free-electron metal obeying Fermi-Dirac statistics. We can compare Eq. (33) directly with Eq. (18) remembering that $\vec{E} = -\vec{\nabla}V$, to obtain the thermopower

$$S = \frac{1}{|e|T} (E_F - \frac{H_2}{H_1}).$$

(35)

In the limit $E_F \gg kT$, Eq. (34) can be solved for H_1 and H_2 by doing a Taylor expansion about E_F. This gives, to second order,

$$S = \frac{-(\pi k)^2 T}{6|e|\tau(E_F)E_F^{1/2}} [\frac{1}{E_F} \frac{d^2}{dE_F^2} (\tau(E_F)E_F^{5/2}) - \frac{d^2}{dE_F^2} (\tau(E_F)E_F^{3/2})]. \quad (36)$$

So we see that the thermopower finally depends on the functional form of $\tau(E)$. If a relation of the form

$$\tau(E) = CE^m.$$

(37)

is assumed, where C is some constant, then Eq. (36) reduces to the form

$$S = \frac{-(\pi k)^2 T}{3|e|E_F} (m + 3/2).$$

(38)

This is the diffusion thermopower S_D of a free-electron metal obeying Fermi-Dirac statistics for which $T_F \gg T$ and in which a single relaxation time exists. If $m = -1$ in Eq. (37), which is expected for $T \gtrsim \theta_D$, then

$$S_D = \frac{-(\pi k)^2 T}{6|e|E_F}.$$

(39)

Experimentally, Eq. (38) is often found to hold at high temperatures but

not at low temperatures where a 'hump' is often observed in the S vs. T relation. This 'hump' can be either positive or negative and often extends to room temperature and sometimes beyond. This effect is attributed to phonon drag and gives an additional term in the thermopower.

In the calculation of the diffusion thermopower, it has been tacitly assumed that the phonon system is in equilibrium at all temperatures while absorbing excess energy and momentum of the electrons falling through a temperature and/or potential gradient. This one-way process occurs only when strong phonon-phonon, boundary or impurity interactions exist. Under these conditions, the lattice is in quasi-equilibrium and with the electron-phonon relaxation time τ, results in Eq. (38). However, a phonon flux can occur at low temperatures because there is less phonon-phonon scattering. If a phonon flux exists, a net additional momentum is imparted to the electrons moving down the temperature gradient. Phonon flow then drags along extra electrons to the cold end, modifying the e.m.f. This is an extra thermopower contribution at low temperatures, called the phonon drag thermopower S_g.

To judge the importance of phonon drag, we need to describe the amount of phonon momentum dissipated into the lattice compared to the electron system. A measure of the importance of phonon drag is the phonon-electron relaxation time τ_{p-e} (not the same as τ) compared with the phonon-other relaxation time τ_{p-x}. We can therefore expect that

$$S_g \sim \frac{\tau_{p-x}}{\tau_{p-x} + \tau_{p-e}} . \tag{40}$$

At high temperatures $(T \gtrsim \theta_D)$ $\tau_{p-e} \gg \tau_{p-x}$ and is relatively temperature

independent because the number of electrons is constant. Also, of course, $\tau_{p-x} \to \tau_{p-p}$ and should be proportional to T^{-1}, since the number of phonons excited at high temperatures is linear with T (Ziman, 1960), so that

$$S_g \sim T^{-1}. \quad \text{(high T)} \tag{41}$$

which appears to be more or less in agreement with experimental observations. Since $S_D \sim T$ in this region, we have $S_g \ll S_D$.

There are two types of phonon-phonon interactions; the N-process ($\vec{g}=0$) in which the phonon energy is redistributed, leaving the net momentum unaltered and the umklapp, U-process ($\vec{g}\neq0$) in which the phonon energy and momentum is redistributed. Thus τ_{p-p} solely refers to the U-processes and Eq. (40) refers to the fraction of dissipated momentum which is imparted to the electrons. Thus, if the electrons are not umklapped, we expect an enhanced negative thermopower because both the electron and phonon flows are in the same direction. However, if an electron is umklapped, its velocity can reverse and the electron will move towards the hot end of the conductor, resulting in a positive thermopower contribution. Therefore, the relative probabilities of U- to N-processes will determine whether S_g is negative or positive. This is illustrated in Figure 3.2(a), (b). If the Fermi surface is not spherical, we can also have N-processes which contribute positively to S_g by having a transition between hole-like states as shown in Figure 3.2(c). Inspection of Figure 3.2 reveals a rule proposed by Ziman. "If the cord $\vec{q}$ passes through an unoccupied region in $\vec{k}$-space, the contribution to S_g is positive, if it passes through an occupied region, it is negative." Furthermore, we need
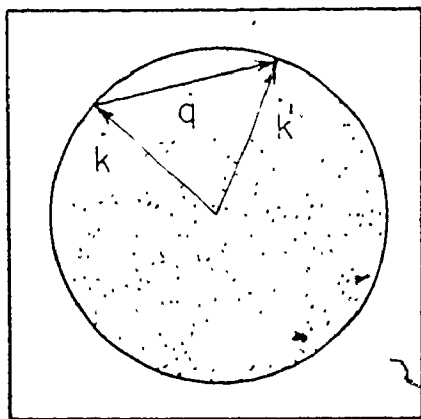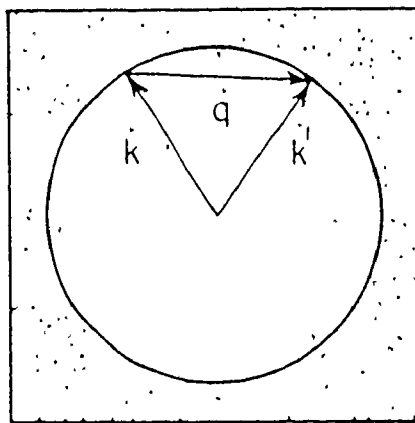
(a)
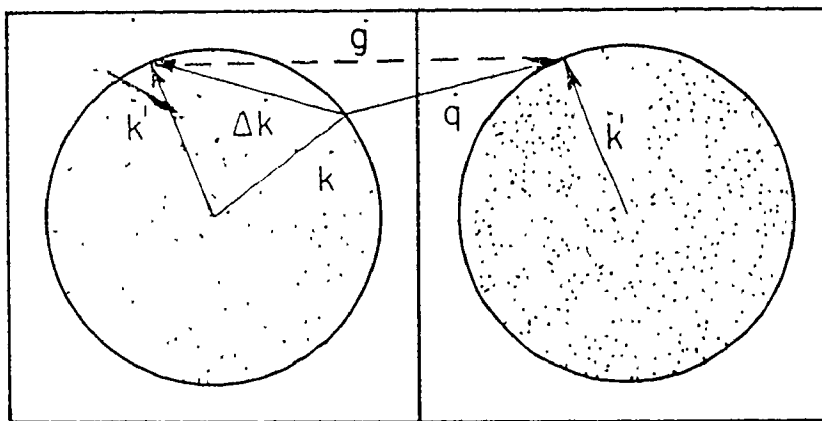
(b)
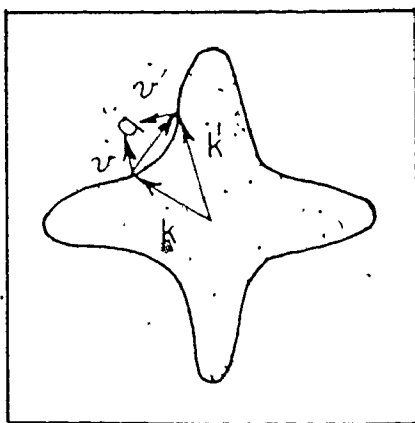
(c)   (d)

to consider the temperature dependence of the U- and N-processes, which are very different from each other. The detailed analysis of this sort of thing is rather complex (Ziman, 1960; Bailyn, 1960), but some of the results are

$$\tau_{p-p} \sim T^{-1}, \quad T \gtrsim \theta_D$$

$$\tau_{p-p} \sim \exp\{\theta_D/2T\}, \quad T << \theta_D$$

$$\tau_{p-e} \sim \text{constant}, \quad T \gtrsim \theta_D \tag{42}$$

$$\tau_{p-e} \sim T^{-1}, \quad T < \theta_D$$

$$S_g^{max} \sim \text{constant}, \quad T \gtrsim \theta_D$$

$$S_g^{max} \sim T^n, \quad T << \theta_D \qquad (n=3 \text{ for n-processes})$$

Using this in conjunction with Eq. (40) allows us to make some predictions about the bahviour of S_g at the temperature extremes. Since S_g increases for $T << \theta_D$ and decreases for $T > \theta_D$, we expect a maximum in S_g somewhere in this temperature range. In fact, this peak is experimentally almost always realized between $0.1\,\theta_D$ and $0.2\,\theta_D$. The magnitude of this peak is very sensitive to the amount of impurities, because any impurity scattering will reduce the amount of phonon momentum imparted to the conduction electrons and therefore reduce S_g.

For the nobel metals S_D is also observed to be positive. This is explained by recognizing the hole-like properties of the Fermi surface as in Figure 3.2(d).

Thus, the thermopower depends on the shape of the Fermi surface and its proximity to the Brillouin zone boundary.

FIGURE 3.2:   Electron-phonon scattering.

(a)   For a N-process S_g is negative since $\Delta \vec{k} = \vec{k} - \vec{k}'$
      is in the same direction as the phonon wave
      vector $\vec{q}$. S_D is negative.

(b)   For a U-process S_g is positive since $\Delta \vec{k}$ is approx-
      imately opposite to $\vec{q}$. S_D is negative.

(c)   For this N-process S_g is positive because
      $\Delta \vec{v} = \vec{v}_k - \vec{v}_{k'}$ is approximately in the opposite
      direction to $\vec{q}$. In other words, the scattering
      is through a hole-like region: S_D is negative.

(d)   In contrast to (a), both S_g and S_D are positive.

CHAPTER IV

Experimental

A. Apparatus

Extreme care is taken to isolate the sample from any possible source of water, due to the extreme hygroscopic nature of the compound. The growth tube (Figure 2.1) is opened inside a dry box, which has a maximum of 10 p.p.m. of water in a nitrogen atmosphere. The sample is mounted as quickly as possible in the sample holder shown in Figure 4.1 and is held firmly in place by two copper rods (7), one of which is spring-loaded. For the experiments, small heaters (2) and (3) on the copper rods heat the sample directly and a larger heater (1) is also provided to heat the whole sample holder. G.E. 7031 varnish is used to provide good thermal contact between the heater wires and the copper and to electrically isolate the thermocouples from the copper rods. The voltage probes (6) are soldered directly onto the rods as close as possible to the thermocouples. Leads are thermally anchored wherever required to minimize unwanted heat flow and thermal gradients, as is indicated in Figure 4.1. The wires passing through the electrical feed-throughs are sealed with 5 min. epoxy which was found to work well, with no leaks developing down to 4.2 K. Finally, a copper can surrounding the sample holder assembly provides an isothermal environment for the sample and also isolation from the atmosphere. The can is threaded at

FIGURE 4.1:   · The sample holder.

 Symbol for thermal anchor

(1)   Heater; 5. of #22 Constantan

(2), (3)   Heaters; 100: of #35 Constantan

(4)   Copper-constantan-copper differential thermocouple

(5)   Copper-constantan thermocouple

(6)   Copper voltage leads

(7)   Copper rods for holding the sample and making thermal and electrical contact to the sample

SPRING

NYLON
SAMPLE
HOLDER

(3)

NYLON
SPACER

(4)

(5)

(7)

(2)

(6)

COPPER CAN

COPPER HEATER BLOCK

CAJON FITTING

FEED THROUGHS

(1)

22
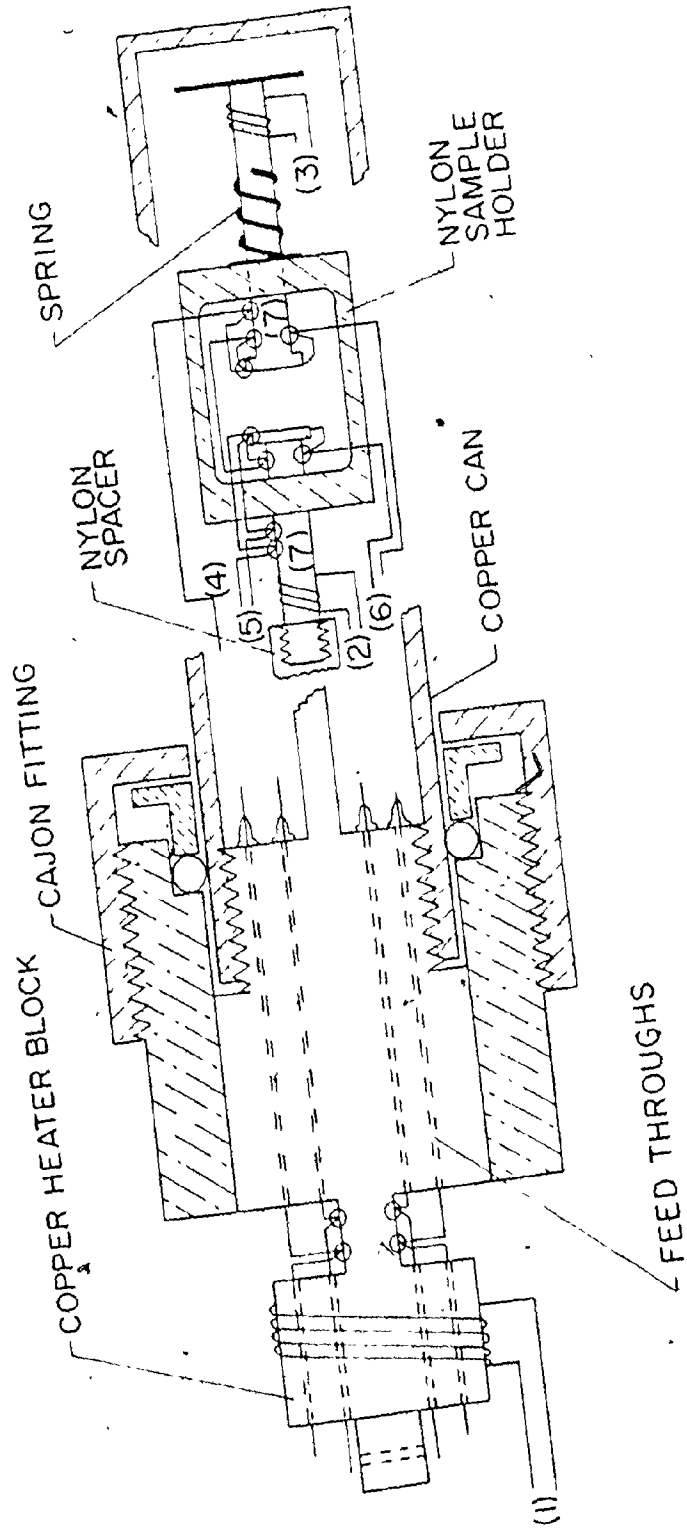
one end so it can be screwed into the copper block for good thermal contact and the o-ring of the cajon fitting provides the vacuum seal at room temperature.

The experimental assembly is shown in Figure 4.2. Electrical connections are made very quickly by means of a gold-plated circuit board connector (17). It was experimentally found that these slide connections did not appreciably increase stray e.m.f.'s in comparison with spot-welded connections. Because the o-ring in Figure 4.1 does not seal at low temperatures, an evacuated stainless steel jacket (21) is used, which has the further advantage of eliminating thermal gradients due to convection currents in such parts as the slide connector (17). Carefully machined and bevelled brass fittings (22) at the top of the stainless steel jacket connect it to the assembly and provide a vacuum seal of at least 10^{-5} torr. A very small amount of silicon grease is used as a lubricant on the seal to make it possible to open the fitting. The heater wires are brought outside the dewar via a 5-pin plug (18), that is epoxied into a swage lock fitting. The voltage and thermocouple wires are brought out through a small section of tubing (19) filled with glyptal cement and clamped tight.

The sample holder and can assembly is put immediately into the dewar which is at nitrogen temperature, as soon as it is removed from the dry box in order to freeze out any moisture. Helium exchange gas can be introduced via (20) to fascilitate cooling at lower temperatures. The electrical apparatus is connected as indicated in Figure 4.2 to provide current to the heaters, measure the e.m.f. and to make temperature measurements.

FIGURE 4.2:   The experimental assembly

         (8)   Keithly 149 Milli-Microvoltmeter

(9), (10)   H.P. 419A D.C. Null Voltmeter

        (11)   H.P. 3450A Digital Voltmeter

        (12)   H.P. 7005B X-Y Recorder

        (13)   10V, 10A Powersupply for heater (1)

        (14)   10V, 100 mA Powersupply for heater (2), (3)

        (15)   Heater switch

        (16)   Reference bath

        (17)   8-pin circuit board connector

        (18)   5-pin connector

        (19)   rubber tube feedthrough and clamp

        (20)   Valve

        (21)   Stainless steel jacket

        (22)   Brass fitting

        (23)   Helium dewar

(20) ⊗ → to pump

(19) (18)

(16)

(23)

(15)

(8) (9) (10)

(22)

(13) (14)

(17)

(11) (12)

(21)
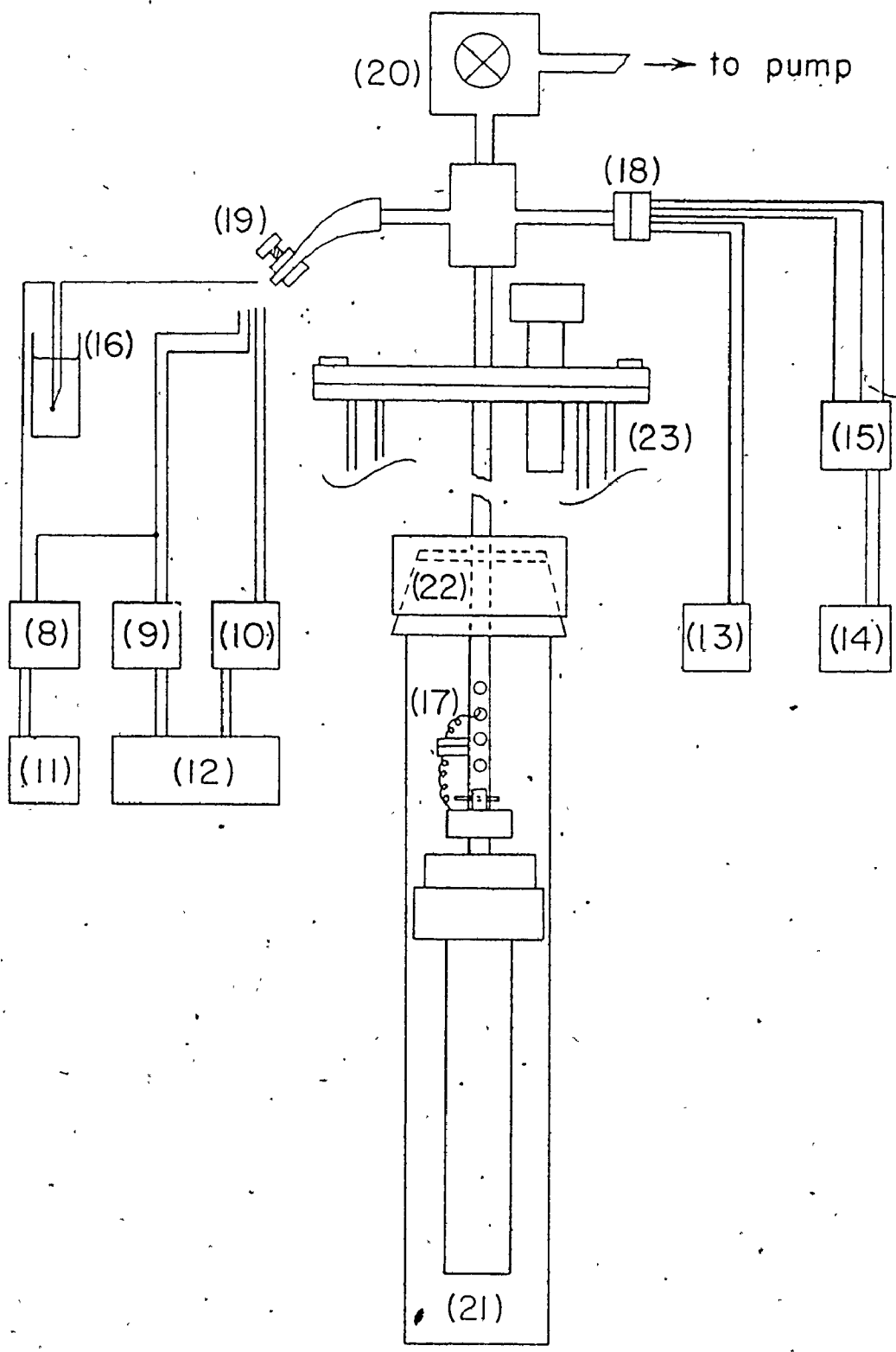
B. Method

The voltage and thermocouple leads attached to the copper rods in close proximity to the sample measure properties of the sample provided that the electrical and thermal conductivities of the sample are much less than that of the copper. Thi̶s condition is satisfied in this experiment with the room temperatu̶r̶e̶ ̶conductivity of $Hg_{2.86}AsF_6$ along the highly conducting direction being about 8×10^3 $(\Omega \cdot cm)^{-1}$ (Cutforth et al., 1975) which is much less than the corresponding conductivity of 6×10^5 $(\Omega \cdot cm)^{-1}$ for copper. The thermal and electrical conductivities are expected to have the same ratio from the Wiedeman-Franz law. This idea and the apparatus were checked out in experiments with lead and nickel pellets of the same size as the $Hg_{2.86}AsF_6$ crystals. We can expect the experimental results for $S_{Hg_{2.86}AsF_6}$ to be considerably more accurate than S_{Cu}, which in turn should be more accurate than S_{Ni} since $\sigma_{Cu}/\sigma_{Hg_{2.86}AsF_6} \sim 70$, $\sigma_{Cu}/\sigma_{Pb} \sim 12$ and $\sigma_{Cu}/\sigma_{Ni} \sim 4$. A further test for the validity of the measured thermopowers can be made by demonstrating that they are independent of sample size.

A particularly convenient choice of a reference material for determining absolute thermopowers is lead. It is a universal standard in thermoelectric measurements because it is commercially available in very high purity and has a small, slowly varying, very accurately known absolute thermopower.

A possible problem of stray thermal e.m.f.'s is eliminated by using a slowly alternating temperature gradient. Referring to Figure 4.1, the voltage is measured while current is first supplied to (2) until the temperature difference is $\frac{1}{2}$°C and then the current is switched by (15) to

heater (3) to produce a temperature difference of about ;°C in the opposite direction. Finally, heater (2) is turned on again until the temperature gradient disappears. This produces a hysteresis curve of ΔV vs. ΔT, in which the hysteresis depends on the rate of heating but the slope is independent of the heating rate. The overall temperature of the sample does not vary by more than about 1°C, so that, providing the thermopower does not vary rapidly in T, the hysteresis curve has linear slopes and forms a closed loop. If the curve does not close on itself, either poor thermal contact between the sample and heater or a change in thermopower with temperature that is too large is at fault and the data are rejected.. A typical trace is shown in Figure 4.3. The measurements thus represent an average thermopower over 1°C → 2°C, for both signs and varying magnitude of the temperature gradient.

The slope of the linear regions of these curves is given by

$$\text{Slope} = \frac{\Delta V}{\Delta T} = \frac{S_{sample} - S_{Cu}}{S_{constantan} - S_{Cu}} \qquad (43)$$

where the denominator is the thermopower of the copper-constantan-copper differential thermocouple (Powell et al., 1961). The thermocouples were calibrated at liquid nitrogen using ice as reference and at liquid helium using liquid nitrogen as reference. The temperatures between the reference points were then adjusted using the linear interpolation

$$V'(T) = V(T) \pm \Delta V_0/\Delta T_0 (T_0 - T) \qquad (44)$$

where T_0 is the reference temperature, ΔV_0 and ΔT_0 the extreme values and V(T) the values given in the reference.

FIGURE 4.3:   A typical trace of the voltage from the sample-
              copper couple (ΔV) vs. the constantan-copper
              couple (ΔT).
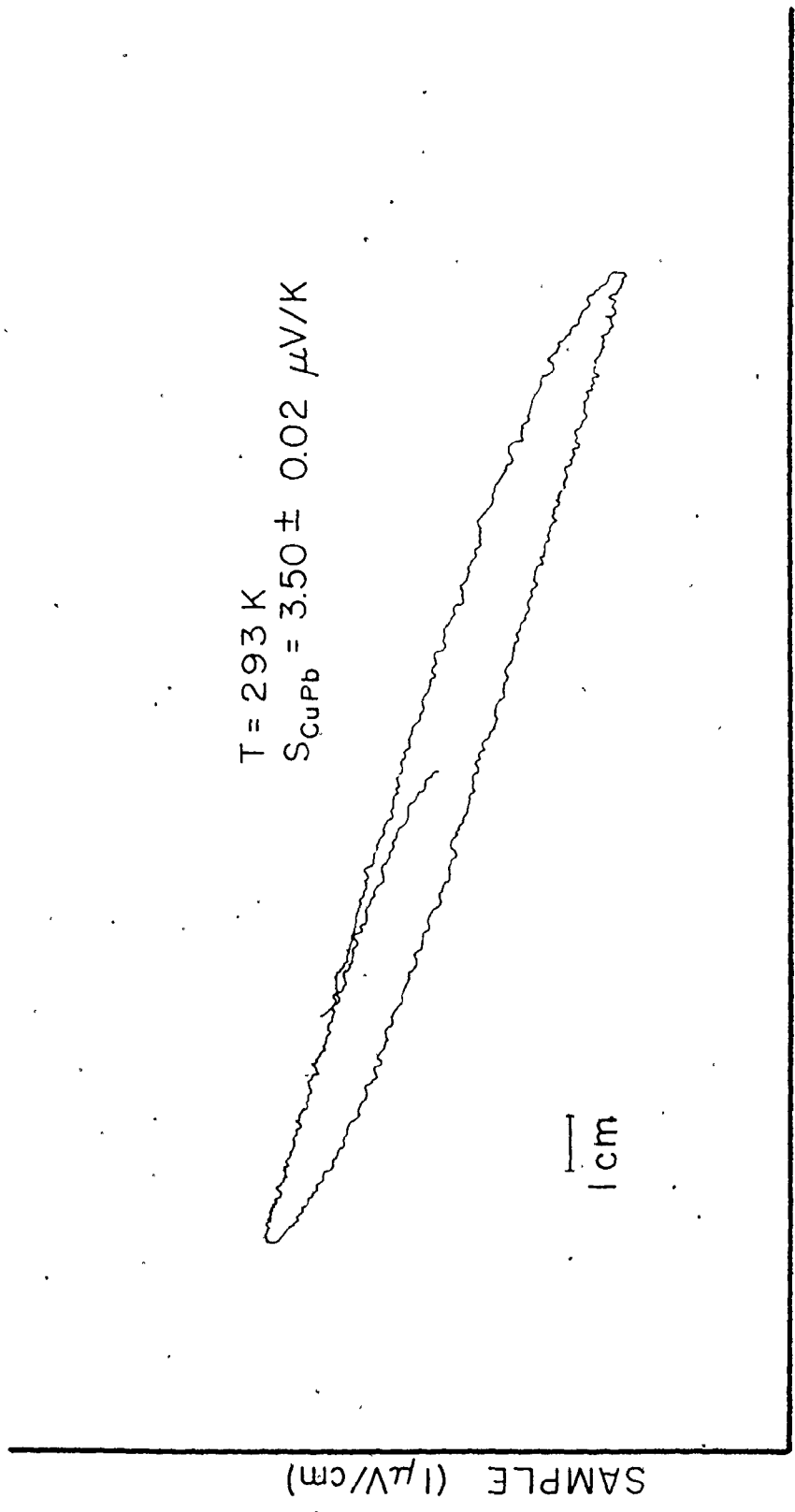
$T = 293\,K$

$S_{CuPb} = 3.50 \pm 0.02\ \mu V/K$

1 cm

THERMOCOUPLE (10·μV/cm)

SAMPLE (1μV/cm)

Since the cooling of the sample is only via radiation, it is very slow. Therefore the helium dewar is pre-cooled with liquid nitrogen so that the $Hg_{2.86}AsF_6$ cools rapidly to about 250 K, below which it seems to be chemically stable. A complete run from room temperature to liquid helium and back to room temperature typically takes two days. Even though this is tediously slow, it has the overwhelming advantage that the sample is always in thermal equilibrium and stray voltages are kept at an absolute minimum. This is of paramount importance since the thermopower of the sample is only fractions of a microvolt per degree Kelvin.

Some anisotropy in the thermopower along the $\hat{c}$ axis ($S_{\hat{c}}$) with respect to the thermopower along the $\hat{a}$ and $\hat{b}$ axes ($S_{\hat{a},\hat{b}}$) for $Hg_{2.86}AsF_6$ is expected because of the anisotropy in the conductivity. For a poly-crystalline sample the net thermopower can be written as (Hübener, 1972)

$$S = \frac{\sigma_{\hat{c}} S_{\hat{c}} + \sigma_{\hat{a},\hat{b}} S_{\hat{a},\hat{b}}}{\sigma_{\hat{c}} + \sigma_{\hat{a},\hat{b}}} \tag{45}$$

but $\sigma_{\hat{c}} \ll \sigma_{\hat{a},\hat{b}}$, so that the thermopower measured for a polycrystalline sample will be approximately $S_{\hat{a},\hat{b}}$. $S_{\hat{c}}$ can be measured directly, because the occasional crystal did grow as a large ($5 \rightarrow 10$ mm^2 by 2 mm) platelet which can be inserted into the holder with the $\hat{c}$ axis along the temperature gradient.

CHAPTER V

Results

The results plotted in Figure 5.1 were obtained for S_{CuPb} using

four lead pellets of about 2 mm diameter and 6 9's grade from Cominco.

Below 30 K, the errors in the thermopower increase considerably until

they become commensurate with the calculated values below about 15 K.

Therefore, below 25 K only the general trend of the thermopower is

indicated by a broken line and no further significance is to be given

to the actual curve. For a particular sample, we get data scatter of

about ± 0.05 $\mu V/K$ and the scatter between different samples is ± 0.2 $\mu V/K$.

In fact, two samples had virtually identical thermopowers. The absolute

thermopower of copper (S_{Cu}) is evaluated by using an averaged value

for S_{CuPb} and subtracting from it S_{Pb} listed in Table 5.1 (Christian

et al., 1958). This result is plotted in Figure 5.2 and includes for

comparison the diffusion thermopower of copper as reported by Pearson

(1961). Using the experimentally determined S_{Cu} values, S_{Ni} is evaluated

from measurements of S_{CuNi}. The form of the temperature dependence is

the same as other published results but the absolute value is low by

approximately 30%.

When mounting the polycrystalline $Hg_{2.86}AsF_6$ crystals, no

problems are encountered as long as they were not exposed to the dry box

atmosphere for more than a day, otherwise the spring tension was enough

to crush the polycrystalline lump. This was taken as direct evidence

. FIGURE 5.1:   Experimental data for S_{CuPb} vs. temperature using

four different samples. The error in the data points

is as follows

120 K $\lesssim$ T $\lesssim$ 300 K	± 0.07 µV/K
60 K $\lesssim$ T $\lesssim$ 120 K	± 0.04 µV/K
30 $\lesssim$ T $\lesssim$ 60 K	± 0.1 µV/K
20 $\lesssim$ T $\lesssim$ 30 K	± 0.2 µV/K

at T $\lesssim$ 20 K the error is ~ 40ꓸ of the measured value

and therefore, the data should not be taken seriously.

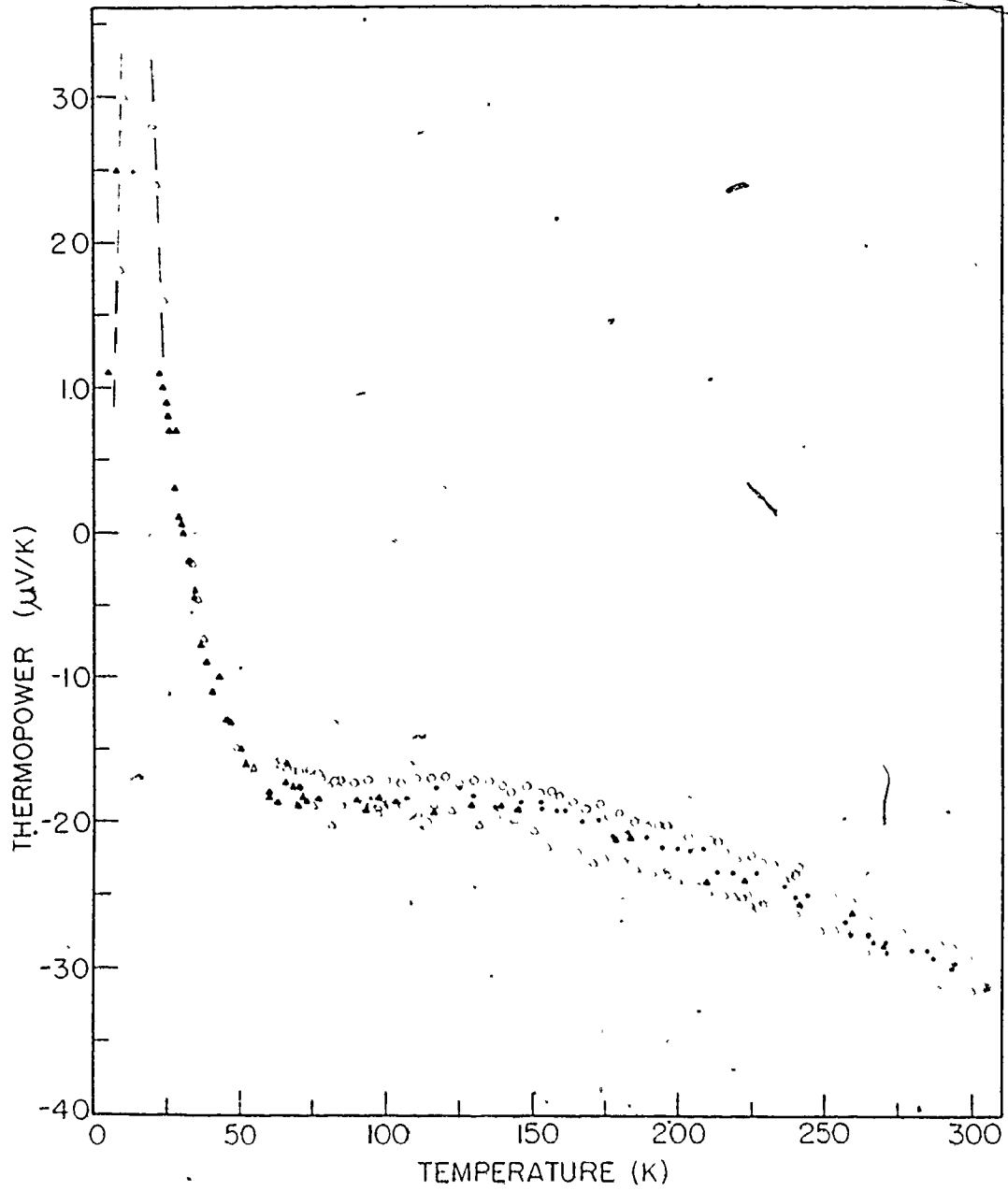TABLE 5.1:   The absolute thermopower of lead after Christian et al.
(1958).

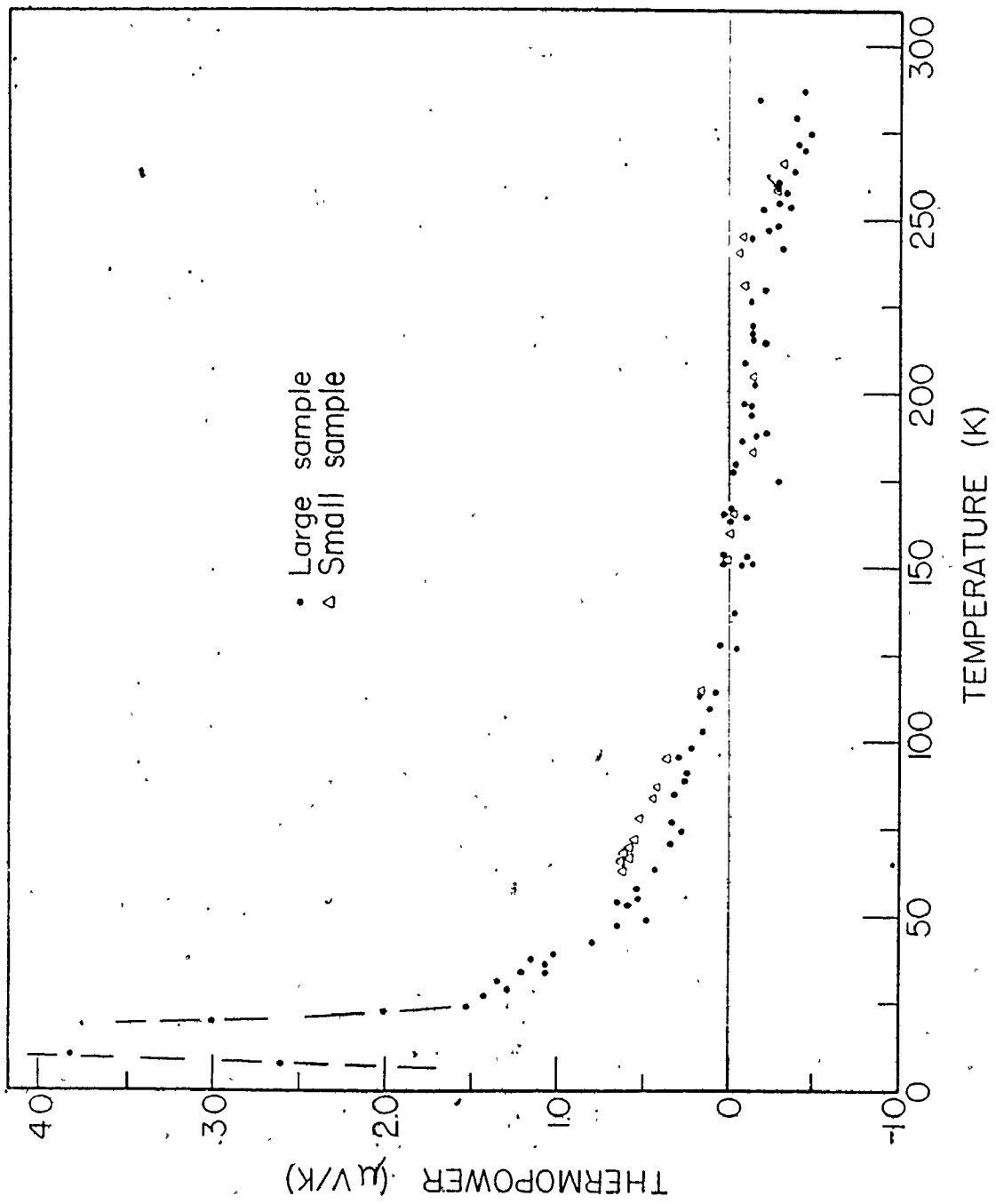| T (K)	S_{Pb} (µV/K)
293.2	-1.27(5)
273.2	-1.25
253.2	-1.21
233.2	-1.18
213.2	-1.15
193.2	-1.10(5)
173.2	-1.06
153.2	-1.02
133.2	-0.96
113.2	-0.91
100	-0.86(5)
90	-0.82(4)
80	-0.79(4)
70	-0.78(4)
60	-0.77(9)
50	-0.77(4)
40	-0.76(4)
30	-0.77(4)
20	-0.73(4)

FIGURE 5.2: An averaged value of S_{Cu} vs. T, obtained by fitting a curve, by eye, to the S_{CuPb} data and adding S_{Pb} from Table 5.1. It is these values for S_{Cu} which are subsequently used in determining S_{Ni} and $S_{Hg_{2.86}AsF_6}$. For comparison in the high temperature region, a typical diffusion thermopower curve as reported by Pearson (1961).
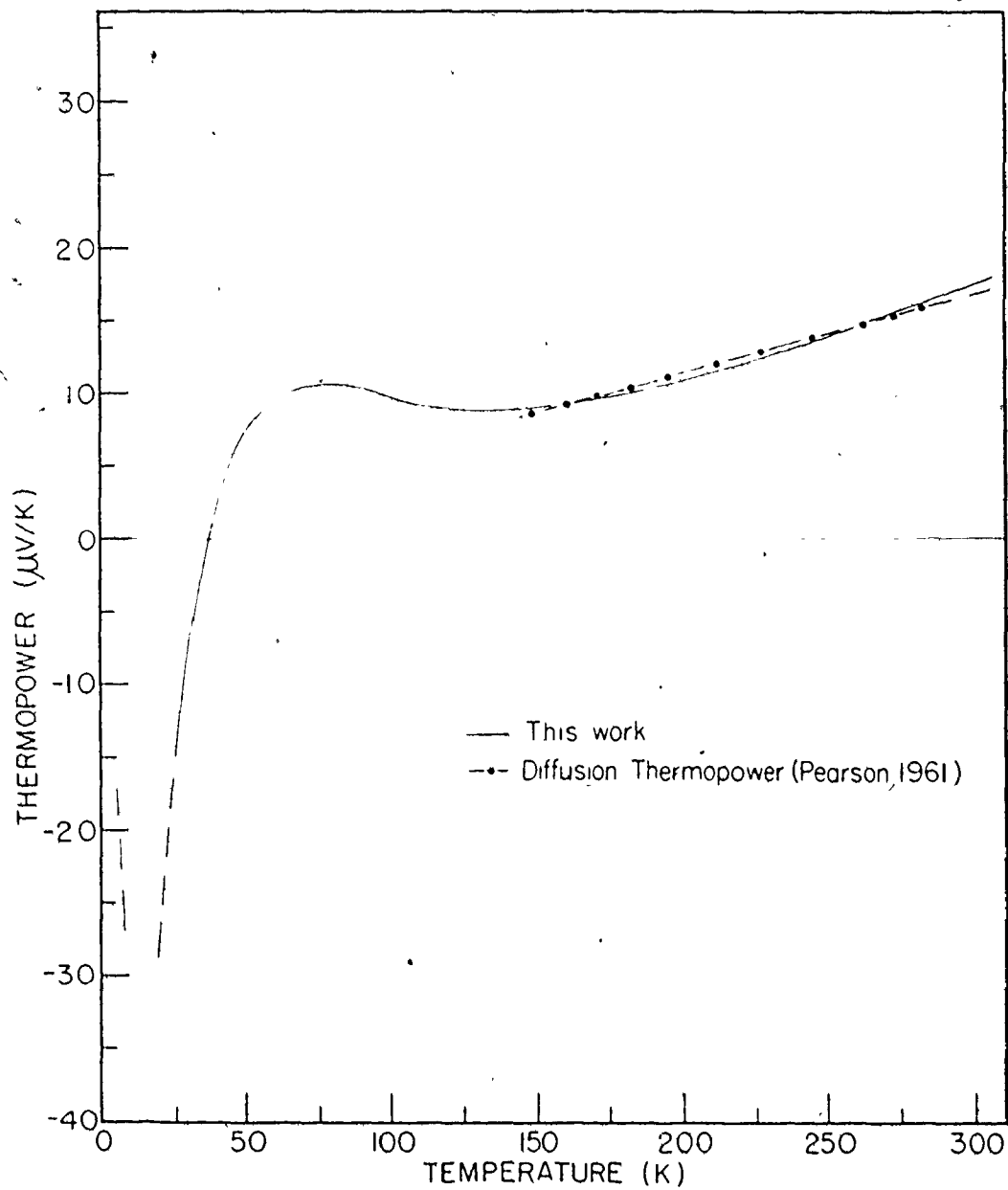
of decomposition even though the crystals still had a golden metallic luster. Altogether four $Hg_{2.86}AsF_6$ lumps were examined and all of them gave identical results. In Figure 5.3, the $S_{\hat{a},b}$ results are plotted for the largest and smallest sample, their length along the temperature gradient differing by a factor of five. During initial temperature cycling, none of the $S_{\hat{a},b}$ results showed any hysteresis or anomalies. However, further cycling eventually brought on a first order transition at 235±2 K to a larger thermopower, which became continually more pronounced with more cycling. The crystals inspected after the transition developed were found decomposed, with surface drops of elemental mercury. The areas, however, where the crystals made contact with the copper rods, were usually still shiny and metallic looking.

Measurements on three platelets were made to determine $S_{\hat{c}}$. Again, results from all crystals were similar and those for the largest are displayed in Figure 5.4. On cooling, all platelets underwent a transition in the temperature range 180 K → 200 K to a smaller thermopower and showed some hysteresis above 90 K on warming. When the samples were cycled again, the original cooling curve was not retraced, but instead the warming curve of the first run was followed. All platelets did show some decomposition on removal from the sample holder and it is suspected that decomposition of the sample is the cause of the hysteresis. No definite results about this could be obtained because of the unavailability of large platelets.

FIGURE 5.3: $S_{\hat{a},\hat{b}}$ vs. T for $Hg_{2.86}AsF_6$. The identical results
               for the small and large samples demonstrate the
               validity of the measuring technique. The negative
               slope at high temperatures indicates that electrons
               are the majority carriers.

THERMOPOWER (μV/K)

TEMPERATURE (K)

• Large sample
△ Small sample

40

30

20

10

0

-10

0   50   100   150   200   250   300

FIGURE 5.4: $S_{\hat{c}}$ vs. T for $Hg_{2.86}AsF_6$. The hysteresis, on
warming above 90 K, is thought to be due to decom-
position of the sample. The positive slope at high
temperatures indicates that holes are the majority
carriers.

THERMOPOWER (μV/K) vs TEMPERATURE (K)

• Cooling
△ Warming
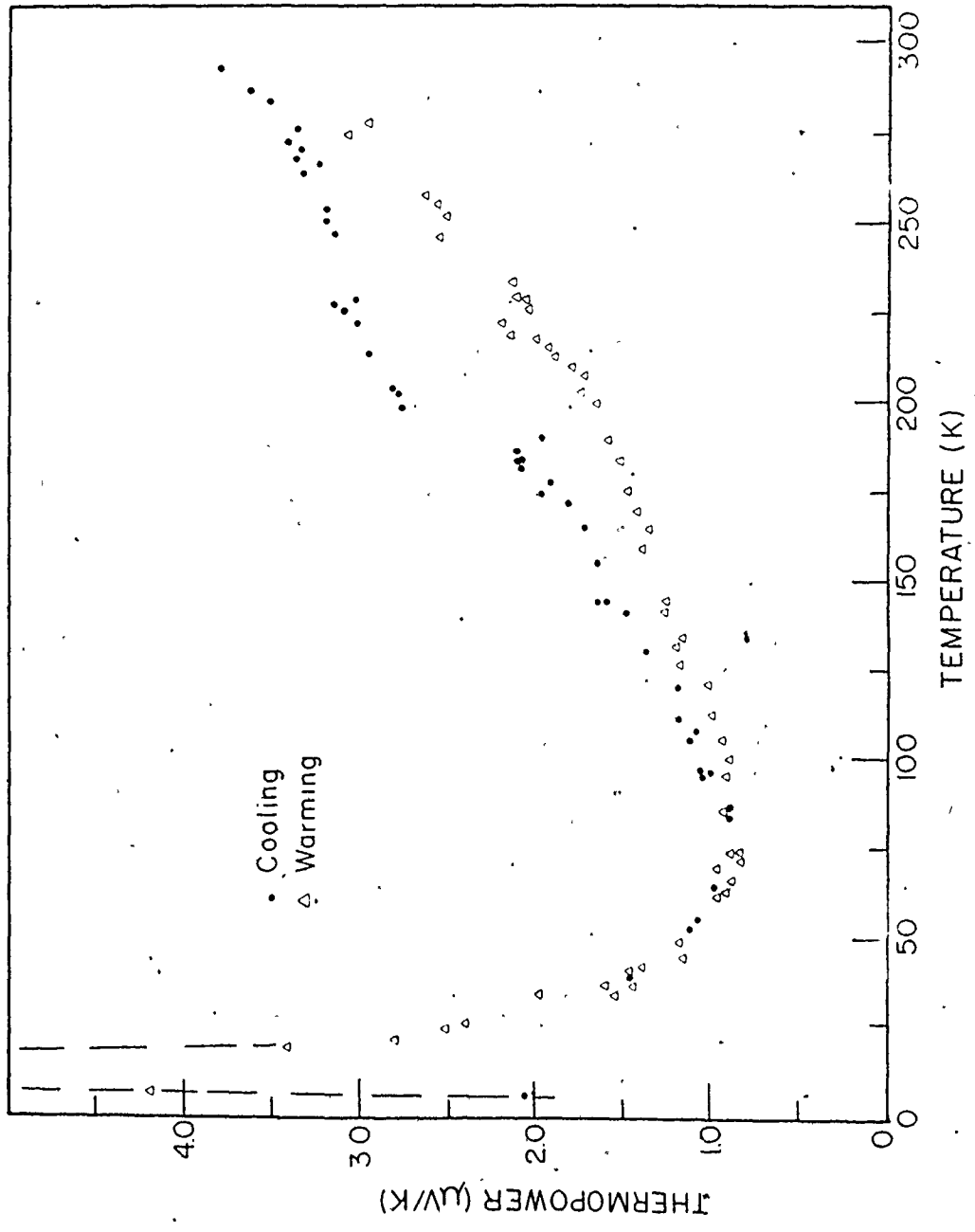
CHAPTER VI.

Discussion

A.. Performance of the thermopower apparatus

The performance of the apparatus using small samples and mechanical contacts is evaluated first because thermopower measurements are usually made with larger samples and with contacts welded to the sample.

The largest error was obtained in the measurement of S_{CuNi} because the conductivity of nickel is almost as large as that of copper so that the temperature gradient across the copper rods, between the differential thermocouple and sample, is an appreciable fraction of the temperature drop across the nickel sample. Therefore, the temperature gradient across nickel is less than that measured, making the thermopower measurements proportionally smaller.

The absolute values of the results for S_{CuPb} (Figure 5.1) are indeed better because the conductivity ratio σ_{Cu}/σ_{Pb} is larger. The systematic variations between results for different lead pellets occur because the conductivity ratio is not large enough to suppress random factors such as sample geometry, surface conditions for electrical and thermal contact, the sample's proximity to the voltage and thermocouple leads, etc. However, when using the average value for S_{CuPb} to calculate S_{Cu} (Figure 5.2), good agreement is obtained with other results (Gold et al., 1960) at all temperatures. In the higher temperature region,

36

the data are in excellent agreement with accepted values of the diffusion thermopower (Pearson et al., 1961). The agreement is good because the impurities in the commercial grade copper will only affect thermopower at low temperatures ($\lesssim$100 K), where impurity scattering and magnetic effects become important. The reason for the systematic increase in the relative error in S_{CuPb} at low temperatures is twofold. First, the thermopower varies rapidly with temperature below 50 K, making small variations in temperature important and, secondly, the sensitivity of the copper-constantan thermocouples below about 25 K is not high.

We may conclude that the method and apparatus used are more than adequate and should give excellent thermopower results for the $Hg_{2.86}AsF_6$ crystals because the conductivity ratio for the $Hg_{2.86}AsF_6$-copper couple is even larger than that of the lead-copper couple. Also, the results of Figure 5.3 indicate that the thermopower measurements are not size dependent, a good indication that the temperature gradient measured is in fact across the sample.

B. Thermopower of $Hg_{2.86}AsF_6$

The thermopower of polycrystalline $Hg_{2.86}AsF_6$ shown in Figure 5.3 is taken to be that along the $\hat{a}$ and $\hat{b}$ directions because Eq. (45) shows that the thermopower of the high conductivity direction is the dominant part of the total thermopower. The thermopower above 120 K varies linearly with temperature and has a negative slope. The intercept of the linear fit to this region is 0.4±0.1 µV/K, which we will have to accept as real since it is just outside the established margin of±0.2 µV/K for systematic errors. However, ignoring this non-zero intercept, the thermopower

behaves like the diffusion term for a degenerate electron gas as predicted by Eq. (38). A fit of the linear thermopower to Eq. (39) gives a Fermi energy of 4.6 ± 0.5 eV for the degenerate electron gas. Batalla (1976) found a value of 6.6 ± 1 eV from optical reflectivity data which, considering surface decomposition problems, is remarkably similar to our value. Another estimate can be obtained from an electron density calculation. Let us assume the $(AsF_6)^-$ octahedra to be spherical with a radius of 2.3 Å (Table 1.1). This reduces the effective volume occupied by the conduction electrons to about 500 $Å^3$, from the unit cell volume of 701.1 $Å^3$, corresponding to a Fermi energy of 4.1 eV assuming 1.65 conduction electrons per mercury atom. These similar values of E_F from these three independent approaches, using the free electron theory as a model, indicate that there is metallic conduction in $Hg_{2.86}AsF_6$.

At 140 ± 30 K the thermopower increases to zero and on further cooling becomes positive, with a maximum at 13 ± 3 K and then decreases to zero at still lower temperatures. This is typical of phonon drag enhancement. However, the positive nature down to relatively low temperatures is unusual.

Some insight into the positive thermopower can be gained by considering the following simplified argument. We consider a particular plane perpendicular to $\hat{c}$ and assume that the mercury atoms form a regular two-dimensional lattice of $\hat{a} = 2.64$ Å and $\hat{b} = 7.54$ Å. Having already established the free electron nature of the compound, we then determine the free electron Fermi surfaces in $\hat{k}$-space as is shown in Figure 6.1. The main feature immediately apparent is the connected surfaces in the first and second Brillouin zones. These surfaces can support umklapp

FIGURE 6.1:   The first, second and third Brillouin zones for

the $\hat{a}$–$\hat{b}$ planes of $Hg_{2.86}AsF_6$. The reciprocal

lattice parameters are $A = 2.38 \overset{\circ}{A}{}^{-1}$, $B = 0.83 \overset{\circ}{A}{}^{-1}$

and corresponding to $E_F = 4.6 \pm 0.5$ eV we calculate

$|k_F| = 1.10 \pm 0.05 \overset{\circ}{A}{}^{-1}$ using the free electron theory.

FIGURE 6.3:   Schematic illustration of some mercury chains.

Along $\hat{a}$ rows A_1 and A_3 eclipse, while A_1 and A_2

are staggered with respect to each other. The

same is true along $\hat{b}$ for the set of rows B_1, B_3

and B_1, B_2 respectively. Thus, current will
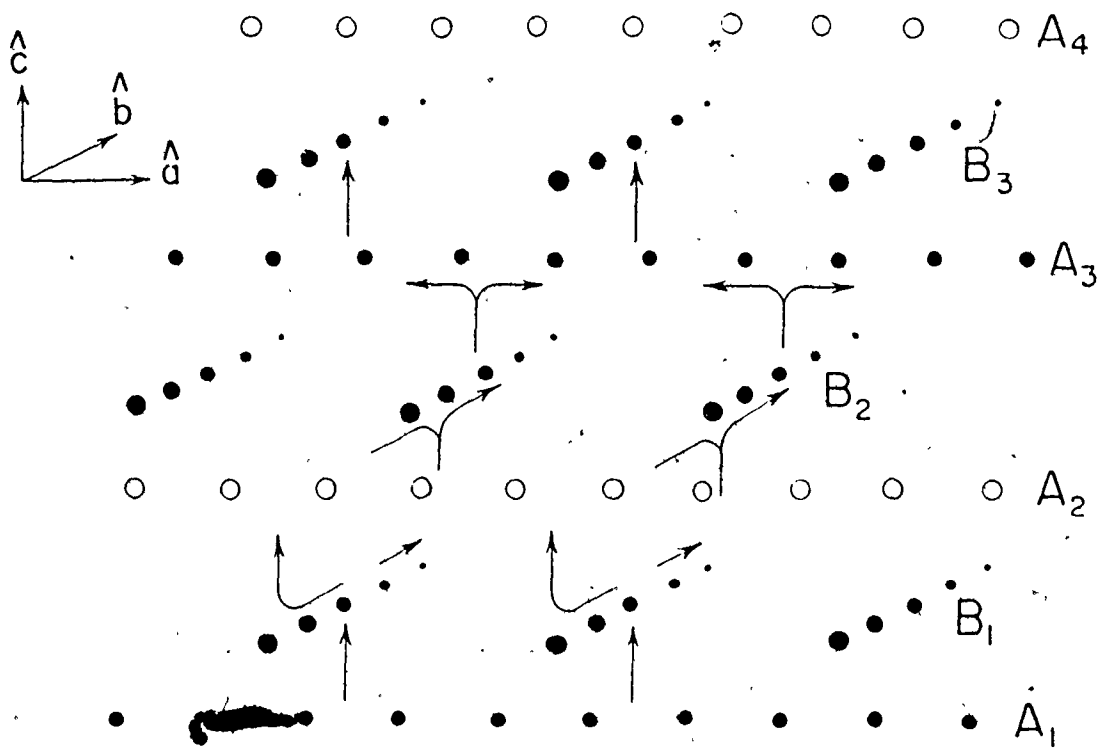
flow in $\hat{c}$ direction wherever A_n, B_n cross.
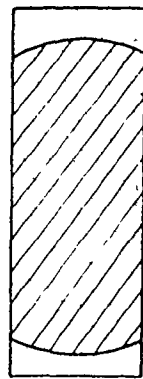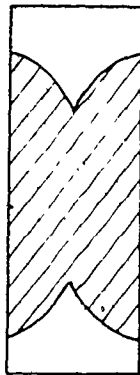
FIRST SECOND THIRD

BRILLOUIN ZONES

$\hat{c}$ $\hat{b}$ $\hat{a}$

A_4

B_3

A_3

B_2

A_2

B_1

A_1
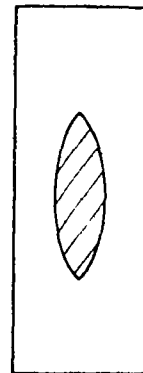
scattering processes down to low temperatures, since part of the Fermi surface is always in contact with the zone boundary and even very small $\vec{q}$'s cause the electrons to umklapp. Referring back to the discussion in Chapter III, a positive phonon-drag component can be expected. In the second zone, the positive phonon drag component is further enhanced by the normal scattering processes across the hole-like regions which, again, can persist to low temperatures because of the narrow Fermi surface width. The lens shape in the third zone contributes a negative thermopower component since it has a positive curvature and is away from the zone boundary. Thus, it seems possible to identify this positive thermopower maximum with phonon drag enhancement. Using Eqs. (40) and (42), we predict a T^{-1} dependence for S_g when $T \gtrsim \theta_D$ and as $T \ll \theta_D$ we expect $S_g \to 0 \ \mu V/K$. In Figure 6.2 S_g, obtained by subtracting the extrapolated S_D component from the total thermopower, is shown to be proportional to T^{-1}. The graph also shows that S_g has disappeared above 100 K, thus restricting θ_D to lower temperatures. However, referring to the discussion in Chapter III, the position of the S_g maxima places θ_D between 50 K and 150 K. Thus θ_D may be compared to that of elemental mercury which is 72 K (Kittel, 1976). A T^{-1} dependence of S_g also results from a semi-conducting behaviour (Tauc, 1962). However, the gradual appearance of a semiconducting gap, due to a metal-semiconductor transition, is not a reasonable explanation of the data because the electrical conductivity of $Hg_{2.86}AsF_6$ samples continuously increases with decreasing temperature.

The first-order transition which develops after the samples have been cycled several times is due to the elemental mercury which is forming because of sample decomposition. At 234 K, the melting point of mercury,

FIGURE 6.2: S_g vs. T^{-1} for $Hg_{2.86}AsF_6$ along $\hat{c}$ axis and $\hat{a},\hat{b}$ axes. S_g is obtained by subtracting the extra-polated S_D values from the total thermopower.

THERMOPOWER (μV/K)

T^{-1} (K^{-1})

$\triangle$ S_g vs T^{-1} for the $\hat{c}$ axis

$\bullet$ S_g vs T^{-1} for the $\hat{a}, \hat{b}$ axis
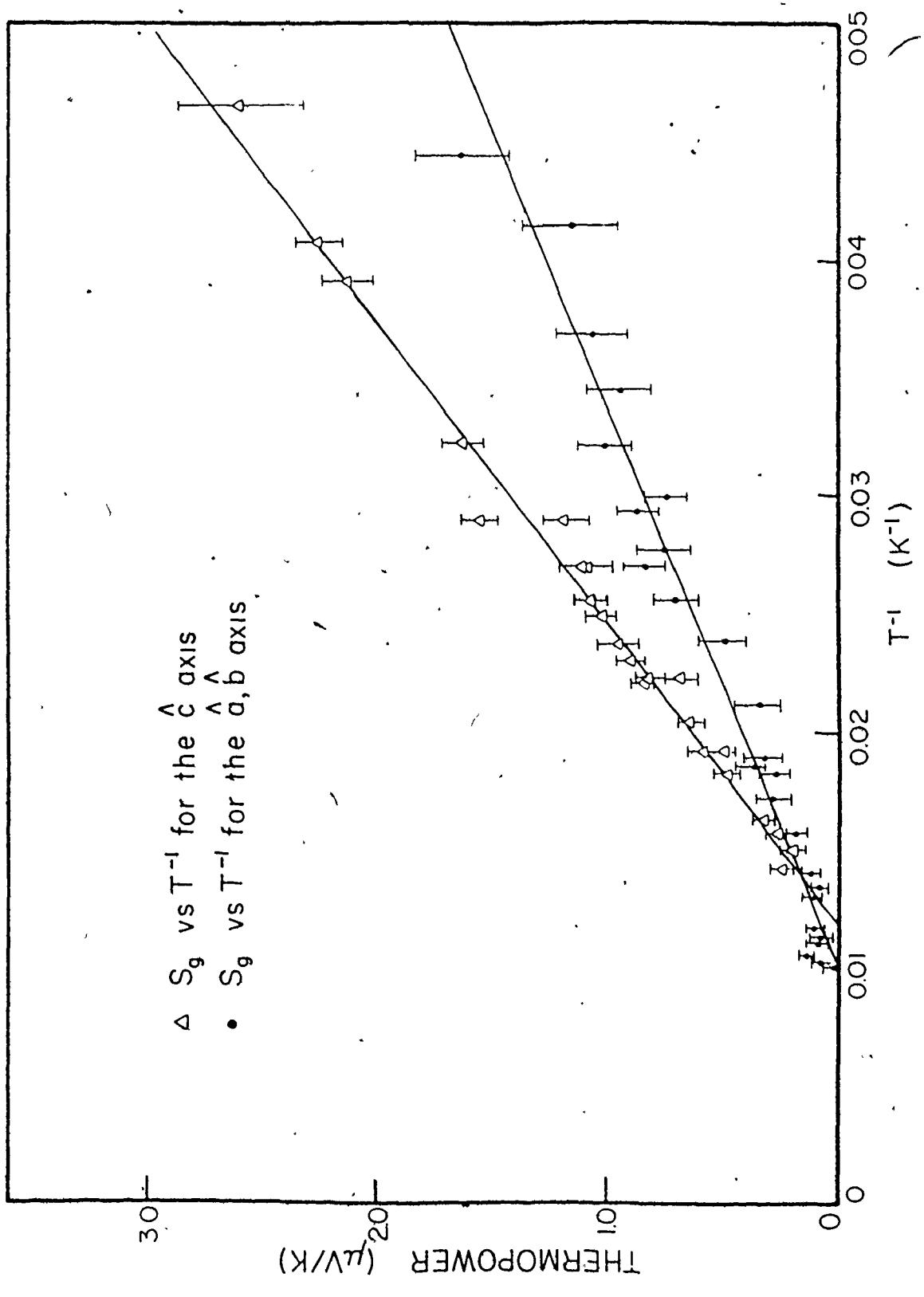
S_{Hg} changes discontinuously from -0.9 μV/K to -4.2 μV/K (Gehlhoff and Neumeier, 1919) on melting. Thus the absence of any transition around 235 K is taken as proof that the sample has not yet deteriorated.

The $Hg_{2.86}AsF_6$ $\hat{c}$ axis thermopower $S_{\hat{c}}$ (Figure 5.4) is quite different from $S_{\hat{a},\hat{b}}$, thus showing the anisotropic nature of $Hg_{2.86}AsF_6$. The temperature dependence of $S_{\hat{c}}$ is linear above 190 K with a positive slope and a non-zero extrapolated intercept. There is evidence of a transition at about 190 K with a 70% decrease in the value of $S_{\hat{c}}$. The temperature dependence is linear immediately below the transition and the linear fit has a slightly larger positive slope and zero intercept within ±0.05 μV/K.

We can attempt to understand the hole-like behaviour from Figure 6.3, where the mercury atoms are illustrated for a repeating unit. It is reasonable to assume that any current in the $\hat{c}$ direction occurs where chains cross, since here the mercury atoms are only separated by ~3.2 Å, compared to ~8.5 Å anywhere else. The arrows in Figure 6.3 attempt to illustrate the expected current flows. Starting at rows A_1 the potential gradient will force the electrons across the ~3.2 Å to the B_1 rows, wherever this set of mutually perpendicular rows approach each other. Next, they flow along B_1 for ~3.7 Å until they can cross to A_2. Then along A_2, again for ~3.7 Å, until they can cross the approximately 3.2 Å to B_2, etc. These twisting paths in the $\hat{c}$ direction cannot, however, be considered as one-dimensional anymore because, due to the many intersections, the electrons are simply not confined anymore to any particular direction. Since the thermopower is anisotropic, we can safely assume that the regions where the electrons cross from one chain to the next,

have the most importance in determining any $\hat{c}$ axis properties. This
consideration makes it tempting to ignore any conduction along the $\hat{a}$
and $\hat{b}$ directions, which is equivalent to translating the A_2, B_2 and
A_4, B_4, etc. rows by 45° in the $\hat{a}$-$\hat{b}$ plane so that all rows eclipse each
other and linear chains form parallel to the $\hat{c}$ axis. Fermi surfaces,
of questionable validity, for this kind of model are indeed found to be
hole-like, but no connectivity is found. Thus, the positive phonon drag
term observed is due to the N-processes in the hole-like regions.
Plotting S_g vs. T^{-1}, we again find a linear fit (Figure 6.2). Similar
to the $\hat{a}$ and $\hat{b}$ directions, S_g disappears at 100 K and this along with
the position of the peak at ~13 K, again fixes θ_D somewhere close to 70 K.

The observed transition indicated in Figure 5.4 is not thought
to be due to elemental mercury, since it would then have to occur close
to 234 K. This transition is also observed in D.T.A. experiments of
van Schyndel et al. (1976) and also in the $\hat{c}$ axis resistivity measurements
of Cutforth et al. (1976), where the change in resistivity is of similar
magnitude to the change in S_c. The transition may well result from an
orderly realignment of the mercury atoms from their somewhat random inter-
chain spacing so that, for example, the distance between atoms from one
row to the next, wherever rows cross, is minimized. This example seems
reasonable, since no anomalies are observed for $S_{a,b}$ in this temperature
range and therefore the transition must be related in some way to the
conduction process from one chain to the next.

Therefore, for $S_{a,b}$ and S_c, there is a gradual transition at
about 100 K from a diffusion dominated thermopower to a phonon drag domi-
nated thermopower, with no indication of any metal-insulator transition.

CHAPTER VII

Conclusion

The conductivity ratio of the two materials in contact in a thermopower experiment is found to be a valid gauge for determining the performance of the apparatus. A ratio of greater than 20 gives acceptable results, which is also verified by showing that the thermopower is not size dependent.

Metallic electron dominated conduction is found along the $\hat{a}$ and $\hat{b}$ directions of $Hg_{2.86}AsF_6$, whereas holes were found to be the majority carriers in the c direction, thus amply confirming the anisotropic nature of the compound.

Free electron theory is found to be a good model for interpreting the thermopower in both of the principal directions. In both cases, the thermopower is well described by $S = S_D + S_g$, with S_g dominating below 100 K. Using this model, the Fermi energy is evaluated at 4.6 ± 0.5 eV; the positive phonon drag thermopower along the $\hat{a}, \hat{b}$ axes is explained by the connectivity in the Fermi surface, which supports umklapp processes; the positive phonon drag thermopower along the $\hat{c}$ axis is shown to be possibly due to N-processes in hole-like regions and a Debye temperature is fixed close to 70 K.

There is a change in the thermopower at 180 K → 200 K along the $\hat{c}$ axis, but not along the $\hat{a}, \hat{b}$ axes. This indicates possible ordering between neighbouring mercury chains, or a change in the crystal lattice along the $\hat{c}$ axis.

BIBLIOGRAPHY

Batlyn, M., Phyl. Mag. $\underline{5}$, 1059 (1960).

Barnard, R.D., "Thermoelectricity in Metals and Alloys", Ch. 3 (1972).

Barret, C.S., Acta Cryst. $\underline{10}$, 58 (1957).

Batalla, E., private communications, (1976).

Brown, I.D., B.D. Cutforth, C.G. Davies, R.J. Gillespie, P.R. Ireland
and J. Vekris, Can. J. Chem. $\underline{52}$, 791 (1974).

Chaikin, P.M., J.F. Kwak, T.E. Jones, A.F. Garito and A.J. Heeger, Phys.
Rev. Lett. $\underline{31}$, 601 (1973).

Christian, J.W., J.P. Jah, W.P. Pearson and I.M. Templeton, Proc. Roy.
Soc. (London) $\underline{A245}$, 213 (1958).

Coleman, L.B., J.J. Cohen, D.J. Sandman, F.G. Yamagishi, A.F. Garito and
A.J. Heeger, Solid State Commun. $\underline{12}$, 1125 (1973).

Cutforth, B.D., W.R. Datars, R.J. Gillespie and A. van Schyndel, Adv.
Chem. $\underline{150}$, 56 (1975).

Cutforth, B.D., W.R. Datars, A. van Schyndel and R.J. Gillespie, Solid
State Commun. (to be published) (1976).

Gehlhoff, G., F. Neumeier, Deutsch. Phys. Gesell., Verh. $\underline{21}$, 201 (1919).

Gold, A.V., D.K.C. MacDonald, W.B. Pearson and I.M. Templeton, Phil.
Mag. $\underline{5}$, 765 (1960).

de Groot, S.R., "Thermodynamics of Irreversible Processes", (1951),
North Holland.

Hübner, R.P., Solid State Physics $\underline{27}$, 63 (1972).

Kwak, J.F., G. Beni, P.M. Chaikin, Phys. Rev. B13, 641 (1976).

Little, W.A., Phys. Rev. 134, A1416 (1964).

Pearson, W.B., Solid State Physics (U.S.S.R.) 3, 1411 (1961).

Peierls, R.E., "Quantum Theory of Solids", p. 108 (1955), Oxford University Press.

Powell, R.L., M.D. Band and R,J. Corruccini, Cryogenics, Vol. I, p. 1 (1961).

Rowe, V.A., P.A. Schröder, J. Phys. Chem. Solids 31, 1 (1970).

van Schyndel, A., W.R. Datars, B.D. Cutforth and R.J. Gillespie, (to be published) (1976).

Schuster, H.G., One-dimensional conductors, Lecture notes in physics 34, New York: Springer-Verlag, (1975).

Tauc, J., "Photo and Thermoelectric Effects in Semiconductors", Ch. 4, (1962), Pergamon Press.

Ziman, I.M., "Electrons and Phonons", (1960), Clarendon Press, Oxford.

Ziman, I.M., "Introduction to Solid State Physics", p. 126, (1976), John Wiley & Sons.